symmetry

MDPI

Article

Investigation on the Formation and Evolution Mechanism of Flow-Resistance-Increasing Vortex of Aero-Engine Labyrinth Based on Entropy Generation Analysis

Xiaojing Liu [1], Shuiting Ding [1,2], Longtao Shao [3], Shuai Zhao [1], Tian Qiu [1], Yu Zhou [1], Xiaozhe Zhang [4,5,*] and Guo Li [3]

[1] Research Institute of Aero-Engine, Aircraft/Engine Integrated System Safety Beijing Key Laboratory, Beihang University, Beijing 100191, China; liuxiaojing@buaa.edu.cn (X.L.); dst@buaa.edu.cn (S.D.); zhaoshuai@buaa.edu.cn (S.Z.); qiutian@buaa.edu.cn (T.Q.); zybuaa@hotmail.com (Y.Z.)
[2] Department of Aviation Engineering, Civil Aviation University of China, Tianjin 300300, China
[3] School of Energy and Power Engineering, Beihang University, Beijing 100191, China; sltwhut@163.com (L.S.); lg666@buaa.edu.cn (G.L.)
[4] Shenyang Engine Research Institute, Aero Engine Corporation of China, Shenyang 110015, China
[5] Aero-Engine Thermal Environment and Structure Key Laboratory of Ministry of Industry and Information Technology, Nanjing University of Aeronautics and Astronautics, Nanjing 210016, China
* Correspondence: xzzmail@foxmail.com

Abstract: Labyrinth seals are widely employed in the air system of aircraft engines since they reduce the leakages occurring between blades and shrouds, which affect the entropy generation significantly. Excessive leakage flow of the labyrinth may be reduced the efficiency and performance of the engine. This paper proposes the concept of flow-resistance-increasing vortex (FRIV) on the top of the labyrinth that is based on the flow entropy generation mechanism of the stepped labyrinth and the main flow characteristics that lead to entropy generation. A three-dimensional simulation model of the labyrinth structure was established, and the model was compared and verified with the experimental data of the reference. The relative dissipation strength and vorticity distribution of the FRIV were theoretically analyzed. It was confirmed that the dissipative intensity distribution was the same as the vorticity distribution, and the correlation coefficient was larger in the labyrinth tip region. Therefore, a parametric study was conducted on design parameters related to the FRIV, including the teeth inclined angle, tooth crest width, step inclined angle, and other parameters. The results are beneficial for the construction of a stronger FRIV to reduce the leakage. This research is of great significance for the improvement of engine efficiency and for the reduction of fuel consumption in the future.

Keywords: labyrinth; flow characteristics; entropy generation; flow-resistance-increasing vortex; correlation coefficient; 3D simulation

check for updates

Citation: Liu, X.; Ding, S.; Shao, L.; Zhao, S.; Qiu, T.; Zhou, Y.; Zhang, X.; Li, G. Investigation on the Formation and Evolution Mechanism of Flow-Resistance-Increasing Vortex of Aero-Engine Labyrinth Based on Entropy Generation Analysis. *Symmetry* **2022**, *14*, 881. https://doi.org/10.3390/sym14050881

Academic Editors: Zheng Xu and Mikhail Sheremet

Received: 28 March 2022
Accepted: 20 April 2022
Published: 25 April 2022

1. Introduction

The labyrinth sealing technology is an important sealing technology in the air system of aero-engines, one that is a non-contact dynamic sealing composed of a rotor and a stator. There is a clearance between the tooth top and the static part, which directly affects the leakage flow of the labyrinth teeth. If the leakage flow rate of the labyrinth teeth is greater than the current design, it may directly reduce the efficiency and performance of the engine, and the maximum efficiency may even be reduced by 10% [1]. On the one hand, the kinetic energy of the fluid is consumed by the sudden expansion and contraction of the flow channel and converted to entropy production. On the other hand, when the rotating parts do work on the contact fluid, it will result in energy loss and entropy generation [2]. In other words, the main factors affecting entropy generation include the total pressure loss and the windage heating.

In the literature, a large number of studies on labyrinth seals can be found concerning experimental tests and numerical and analytical models. In terms of theoretical research, Martin first proposed the calculation method of the flow rate of the labyrinth teeth. The labyrinth tooth is regarded as a series of holes, and the fluid is assumed to be in an isothermal flow. However, this method is only suitable for incompressible streams, and the calculation error is large [3]. Then, Vermes revised the calculation formula proposed by Martin and added the correction term [4]. Zimmermann put forward a relational formula for calculating the carry factor or residual energy factor in the leakage flow rate of the labyrinth by means of experiments [5]. These theories are the basis for the research on the leakage of the labyrinth teeth. In terms of numerical research, the processing power of modern computers allows indeed for the simulation of more complex and detailed phenomena than that of the past years. On the basis of the experimental data of Waschka et al., Nayak et al. used a numerical simulation to study the effect of rotational speed on the sealing performance of the labyrinth teeth [6]. Lee et al. reviewed and summarized the literature on the grate seal structure since the 1960s, discussing the effect of sealing parameters on leakage flow [7]. Soemarwoto analyzed the flow mechanism of stepped teeth and stepped helical teeth by numerical simulation, and further studied the effect of tooth height on the vortex [8]. Rhode and Demko conducted a numerical study on the straight-through grate sealing structure by the finite difference method [9,10]. Stoff calculated the incompressible flow inside the straight-through labyrinth seal structure by the standard $k - \varepsilon$ turbulence model and analyzed the relationship between the leakage of the labyrinth structure and the pressure gradient [11]. Rhode and Sobolik et al. modified the standard $k - \varepsilon$ turbulence model by introducing the effective viscosity coefficient and studied the compressible flow in the straight-through labyrinth seal structure [12]. Rhode and Hibbs analyzed the effect of dimensional structure changes on the sealing performance of the labyrinth structure [13,14]. Demko and Morrison studied the effect of rotational speed on the flow of the straight-through labyrinth seal structure by numerical method [15]. Rapisarda et al. studied the influence of step position and tooth edge on leakage coefficient by using the numerical method and obtained the influence law of windage heating and vortices on leakage [16,17]. Kali charan Nvayak et al. studied the windage heating characteristics of the grooved stepped tooth-honeycomb bushing labyrinth seal structure by numerical method [18,19]. Kaliraj et al. analyzed static and rotational effects of labyrinth seals at various flows and geometrical dimensions and optimized leak flow by straight and steeped seal configurations [20]. Desando and Rapisarda focused on the implementation of a numerical model for rotating stepped labyrinth seals installed in low-pressure turbines [21]. Ganine presented a simplified coupled transient analysis methodology that allows for the assessment of the aerothermal and thermomechanical responses of engine components together with cooling air mass flow and pressure and temperature distributions in an automatic fully integrated way [22]. In the experimental research, Child provided an overview of the development of vortices in labyrinth seals and their main effects on self-excited instability [23]. Wittig et al. measured the leakage characteristics of the through-grate plane model under different pressure ratios and Reynolds through experiments, showing the influence of basic aerodynamic parameters on the through-grate flow coefficient [24]. Denecke et al. analyzed the influence of the inlet swirl on the windage heating and swirl development of the simple grate segment, which compared the experimental results with the calculation results McGreehan and Ko [25]. The results show that the local circumferential velocity and the development of the swirl in the grate flow channel are the key factors affecting the accuracy of the temperature rise calculation [26]. Willenboge et al. studied the influence of Reynolds number and inlet and outlet pressure ratio on the leakage characteristics of stepped grate structure through experiments, which showed that at a high Reynolds number, the flow coefficient may have a local maximum value [27]. Stocker and Rhode et al. studied the effect of the relative position of the wear groove and the axial direction of the labyrinth on the leakage characteristics of the labyrinth seal through experiments [28,29]. Millward and Edward studied the variation law of the heat generated by the wind resistance with the leakage amount and the pressure ratio under different labyrinth tooth structures [30]. Woschka et al. focused on analyzing the effect of rotational speed on head clearance, which showed that rotational speed has a great influence on the head clearance of labyrinth teeth [31]. Braun et al. accurately measured the tooth tip clearance with a static plane labyrinth tooth test bench and showed the effects of pressure ratio and tip clearance on the leakage characteristics of straight and stepped teeth [32]. Min et al. evaluated the leakage characteristics of a stepped labyrinth seal by experiments and computational fluid dynamics [33]. Khan et al. investigated the physical behaviors of heat and mass transfer flow with entropy generation through the effects of embedded parameters [34]. Ramzan et al. reached the conclusion that the entropy generation is increased with the enhancement of radiation parameter, Eckert number, Lewis number, temperature difference parameter, dimensionless constant parameter, Curie temperature, Prandtl number, and concentration difference parameter [35]. Although a large amount of work has been done on the research of labyrinth teeth, hardly anyone has investigated the characteristics of the labyrinth teeth region by the theoretical of entropy generation, which shows energy distribution accurately [36].

Labyrinth sealing technology is becoming increasingly more important in improving the performance of the engine with the advancement of materials and process technology. In practical engineering applications, the flow in the labyrinth seal area is very complicated and there is energy loss. Using the entropy production theory to conduct in-depth research on the flow characteristics of the stepped grate, the energy in this area can be quantitatively analyzed. In this work, flow analysis and reconstruction are performed on the grate region. A method is proposed to construct stronger flow resistance, increasing vortices and reducing leakage by enhancing the labyrinth tip velocity gradient and throttling effect. This research can serve as an important reference for the design and application of aero-engine labyrinth and plays an important role in reducing the kerosene consumption and improving thermal efficiency. The rest of this paper is organized as follows. In Section 2, the flow-resistance-increasing vortex (FRIV) on the top of the labyrinth tooth is introduced, and the leakage characteristics of the labyrinth tooth region are studied on the basis of the theory of entropy production. In Section 3, the labyrinth simulation model is established and checked. In Section 4, the simulation results are analyzed and compared with numerical calculations, which shows that the method proposed in this paper to reduce the leakage of the labyrinth is effective. The last section presents the conclusions of this research.

2. The Formation Mechanism of the FRIV at the Tip of the Labyrinth Tooth

2.1. Definition of Flow-Resistance-Increasing Vortices

The labyrinth structure is widely used in the air system of the engine, which is mainly composed of the turntable and the stator casing. The working principle of a labyrinth seal consists of separating regions at different pressures through the clearance, i.e., a gap placed between rotating and stationary components [37]. In this gap, the conversion of pressure energy into kinetic energy occurs. The latter can then be dissipated into thermal energy into the cavity downstream of the clearance or transferred to the next gap through the kinetic carryover [38]. This labyrinth seal adopted in the present work is a stepped type, with five labyrinth teeth [39]. It can be seen from Figure 1 that there is a vortex in the area behind the labyrinth teeth and another vortex structure in the labyrinth cavity. The vortex can hinder the airflow of the labyrinth tip, and we define the vortex as a flow-resistance-increasing vortices. The labyrinth geometric parameters and their representative symbols are shown in Table 1.

2.2. Theoretical of Entropy Generation

In this work, we focused on the sealing characteristics of the labyrinth; therefore, the system is partially simplified. The flow in the labyrinth is assumed to be steady, viscous, adiabatic, and compressible, and thermal conductivity λ and rotational speed n are not considered. Theoretically, the labyrinth structure of an aero-engine can be regarded as an adiabatic continuous power system. The theoretical deduction process of the entropy generation about aero-engine system is shown as follows, which includes viscous dissipation, heat transfer with temperature difference, metal friction, and mixing.

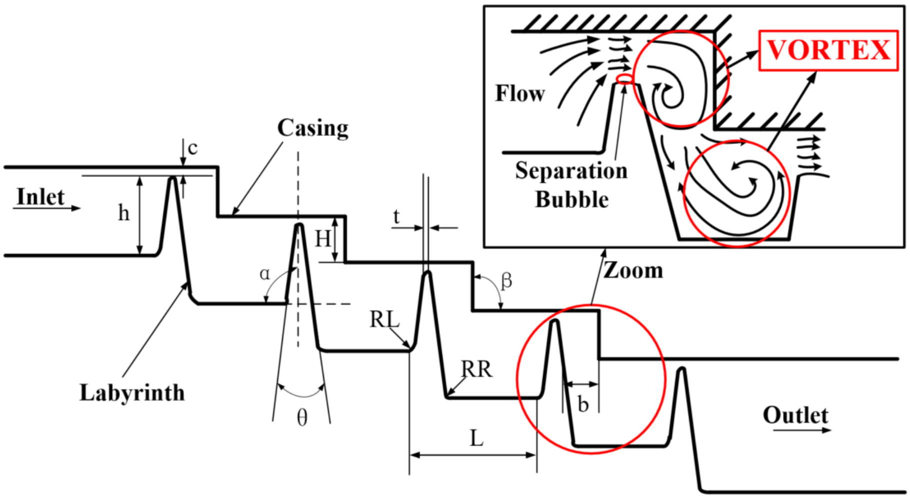

Figure 1. Geometrical dimension drawing of labyrinth seal structure.

Table 1. Symbols and initial values of labyrinth geometric parameters.

Geometric Parameters	Symbol	Initial Value	Unit
Step height	H	2	mm
Teeth pitch	L	7	mm
Tooth height	h	5	mm
Tooth tip width	t	0.3	mm
Labyrinth inclination angle	α	90	degrees
Angle between face teeth	θ	15	degrees
Seal clearance	c	0.36	mm
Tooth to step distance	b	2	mm
Step inclined angle	β	90	degrees
Root rounding of steps	R1	0	mm
Root rounding on pressure side	RL	0.5	mm
Fin tip fillet	RR	0.5	mm

The entropy equation of the open system [40] is as follows:

$$\delta S_g = dS_{CV} - \frac{\delta Q}{T_r} + s_2 \delta m_2 - s_1 \delta m_1 \tag{1}$$

where S_g is the entropy generation; T_r is the wall temperature; Q is the amount of heat exchange; s_2, s_1 is the specific entropy; m_1, m_2 is the mass flow; and S_{CV} is the total entropy of the stable flow system.

For steady flow, adiabatic systems are as follows:

$$dS_{CV} = 0, \frac{\delta Q}{T_r} = 0 \tag{2}$$

For the unit mass working medium, introduce Equation (2) into Equation (1), and the entropy generation equation is simplified to

$$s_g = s_2 - s_1 \tag{3}$$

The energy equation is as follows [41]:

$$-w_s = h_2 - h_1 + \frac{V_2^2 - V_1^2}{2} = h_2^* - h_1^* = c_p(T_2^* - T_1^*) \tag{4}$$

where h_1 denotes import specific enthalpy, h_2 denotes export specific enthalpy, h_1^* denotes total import enthalpy, h_2^* denotes total export enthalpy, T_1^* denotes total inlet temperature, T_2^* denotes total outlet temperature, and c_p denotes constant pressure specific heat.

For a labyrinth in an air system, the entropy generation of the system can be expressed as follows [42]:

$$s_g = s_2 - s_1 = c_p \ln\frac{T_2}{T_1} - R\ln\frac{P_2}{P_1} = c_p \ln\frac{T_2^*}{T_1^*} - R\ln\frac{P_2^*}{P_1^*} \tag{5}$$

$$s_g = c_p \ln\frac{T_2^*}{T_1^*} - R\ln\pi \tag{6}$$

where T_1 denotes inlet static temperature, T_2 denotes outlet static temperature, P_1 denotes inlet static pressure, P_2 denotes outlet static pressure, P_1^* denotes inlet total pressure, P_2^* denotes outlet total pressure, T_1^* denotes inlet total temperature, T_2^* denotes outlet total temperature, c_p denotes constant pressure specific heat, and R denotes general gas constant.

For the windage heating, it is mainly caused by friction:

$$w_s = M\omega \tag{7}$$

where M denotes the frictional force, ω denotes the rotational angular velocity, and w_s denotes the frictional power.

The dimensionless parameters such as the discharge coefficient and windage heating can be expressed as follows [43]:

$$C_m = \frac{M}{0.5\rho\omega^2 r^5} \tag{8}$$

$$w_s = 0.5C_m\rho\omega^3 r^5 \tag{9}$$

$$w_s = \dot{m}c_p\Delta T^* \tag{10}$$

$$\Delta T^* = \frac{C_m\rho\omega^3 r^5}{2\dot{m}c_P} \tag{11}$$

$$\frac{\dot{m}\sqrt{T^*}}{P^*} = f(\pi) \tag{12}$$

$$\Delta T^* = T_2^* - T_1^* = \frac{C_m\rho\omega^3 r^5\sqrt{T_1^*}}{2cpf(\pi)P_1^*} \tag{13}$$

The dissipative entropy generation in the flow originates from the dissipation generated by the viscosity of the fluid, resulting in the irreversible conversion of mechanical energy to internal energy. The equation of the relative dissipation intensity of the fluid micro-element is as follows [44]:

$$\begin{aligned}\phi = {} & \left[2\left(\frac{\partial V_x}{\partial x}\right)^2 + 2\left(\frac{\partial V_y}{\partial y}\right)^2 + 2\left(\frac{\partial V_z}{\partial z}\right)^2 + \left(\frac{\partial V_y}{\partial x} + \frac{\partial V_x}{\partial y}\right)^2 + \left(\frac{\partial V_z}{\partial y} + \frac{\partial V_y}{\partial z}\right)^2 + \left(\frac{\partial V_x}{\partial z} + \frac{\partial V_z}{\partial x}\right)^2\right] \\ & -\frac{2}{3}\left(\frac{\partial V_x}{\partial x} + \frac{\partial V_y}{\partial y} + \frac{\partial V_z}{\partial z}\right)^2\end{aligned} \tag{14}$$

Flow vorticity can be written as

$$\begin{cases} \omega_x = \frac{1}{2}\left(\frac{\partial V_z}{\partial y} - \frac{\partial V_y}{\partial z}\right) \\ \omega_y = \frac{1}{2}\left(\frac{\partial V_x}{\partial z} - \frac{\partial V_z}{\partial x}\right) \\ \omega_z = \frac{1}{2}\left(\frac{\partial V_y}{\partial x} - \frac{\partial V_x}{\partial y}\right) \end{cases} \tag{15}$$

where $V_x,\ V_y,\ V_z$ are the flow velocities in the x, y, and z directions, respectively.

In order to investigate the correlation between the vorticity and the relative dissipation intensity distribution, the correlation coefficient τ is defined as follows [45]:

$$\tau = \omega \cdot \phi \tag{16}$$

Introduce the vorticity transport equation [46]:

$$\frac{Dw}{Dt} = (\omega \bullet \nabla)V - \omega(\nabla \bullet V) + \nabla\rho \times \frac{\nabla p}{\rho^2} + v\nabla^2\omega \tag{17}$$

where $(\omega \bullet \nabla)V$ denotes the stretching and bending of the vortex line caused by the velocity gradient of the flow field, which causes the velocity gradient in the flow field to change significantly and results in a change in the absolute value of the vorticity; $\omega(\nabla \bullet V)$ denotes the change in the magnitude of the vorticity caused by the volume change of the fluid micelle, which causes the absolute value of the vorticity to change; and $\nabla\rho \times \nabla p/\rho^2$ denotes the effect of baroclinic moment on vorticity due to non-parallel pressure gradients and density gradients. For a positive pressure fluid, whose density is only a function of pressure, and thus the density and pressure terms have the same gradient, this term is equal to 0, where $v\nabla^2\omega$ denotes the viscous diffusion effect of vorticity. It can be seen that the first two items in the equation are the main reasons for the generation of the FRIV.

In conclusion, the local entropy generation of the labyrinth can be expressed as

$$s_g = c_p \ln\left(1 + \frac{C_m \rho \omega^3 r^5}{2c_P f(\pi) P_1^* \sqrt{T_1^*}}\right) - R \ln \pi \tag{18}$$

It can be seen that the major local entropy increase comes from the windage heating and the total pressure loss in the flow of the labyrinth.

3. Simulation Model and Verification of Labyrinth

In this section, the labyrinth model is established for simulation and was checked with the known experimental data. In the following sections, the simulation results and theoretical calculations are compared and analyzed.

3.1. Numerical Approach and Computational Meshing

In this paper, UG parametric modeling was adopted, and the step labyrinth and bushing are both axisymmetric. ANSYS CFX (ver. 19.0, ANSYS Inc., Canonsburg, PA, USA, 2018) [47], a commercial software program, was used for CFD analysis. Figure 2 shows the diagram of meshes, Figure 3 shows the diagram of local mesh refinement in the tip of the labyrinth that is critical for investigation [48]. Nevertheless, we ensured that the 3D was practically close to the 2D domain by setting the smallest width as far as we could and applied symmetry conditions to lateral faces. In order to reduce the amount of calculation, a two-dimensional axisymmetric (rotational) model was adopted; this method is recommended for 2D calculations according to the CFX manual [49]. ANSYS ICEM is used for unstructured meshing. ANSYS Fluent is used for the calculation, the inlet and outlet set as the pressure control, and the wall set as non-slip adiabatic. The 3D unsteady compressible N-S equation is solved by the finite volume method. The turbulence is modeled with the $k - \varepsilon$ model with a second-order upwind discretization scheme in time and space.

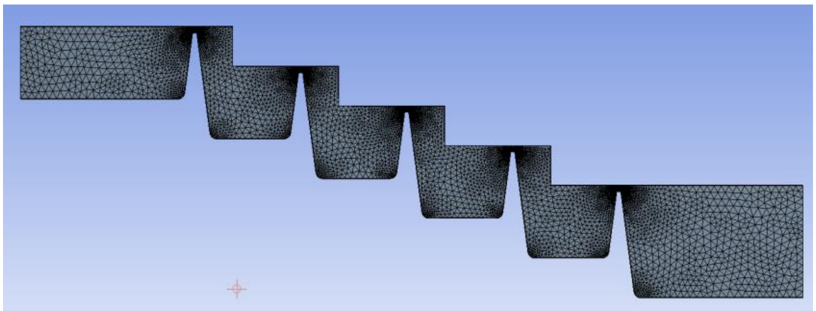

Figure 2. Diagram of meshes.

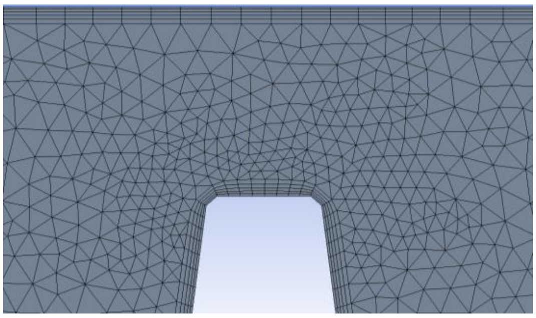

Figure 3. Diagram of local mesh refinement.

3.2. Boundary Conditions and Mesh Independent

Inlet temperature and outlet static pressure and temperature were used as boundary conditions to simulate the operating conditions of the test. Table 2 shows the boundary conditions.

Table 2. Boundary conditions.

Boundary Conditions	Value	Unit
Outlet pressure	101,325	Pa
Import and export pressure ratio	1.5	
Inlet temperature	300	K
Outlet temperature	300	K

Define the inlet and outlet pressure ratio as

$$\pi = \frac{P_2^*}{P_1^*} \tag{19}$$

where converted flow is calculated as follows:

$$\varphi = \frac{m\sqrt{T_1^*}}{P_1^* A} \tag{20}$$

There are two parameters that affect the number of grids and the calculation results in the mesh settings: global minimum mesh size and the minimum mesh size for local refinement of tooth tips. The mesh-independent calculation will be performed for different values of the parameters.

The global minimum mesh sizes were set as 2, 0.6, and 0.2 mm for three working conditions, and the minimum mesh size for local refinement of tooth tips was set as 0.03 mm. The grid numbers corresponding to the three working conditions were 180,000, 190,000, and 360,000. It can be seen from Figure 4 that the flow rate of the grate remained stable with global minimum mesh size varying from 0.2 to 2 mm. In this research, the global minimum mesh size was set as 0.6 mm.

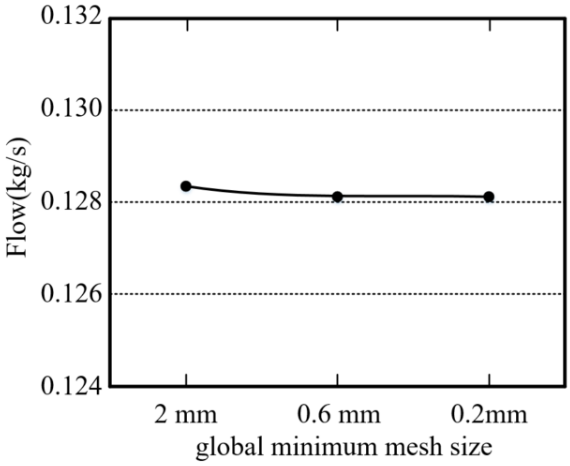

Figure 4. Global minimum mesh independent computation.

The minimum mesh size for local refinement of tooth tips was set as 0.1, 0.03, 0.02, and 0.01 mm for four working conditions, and the global minimum mesh size was set as 0.6 mm. The grid numbers corresponding to the four working conditions were 180,000, 200,000, 320,000, and 710,000. It can be seen from Figure 5, that when the minimum size of the refined mesh of the tooth tip was reduced to 0.03 mm, the flow rate of the labyrinth did not change significantly. Therefore, the minimum size of the local refined mesh of the tooth tip region in the CFD model was set as 0.03 mm, and the number of grids was around 200,000.

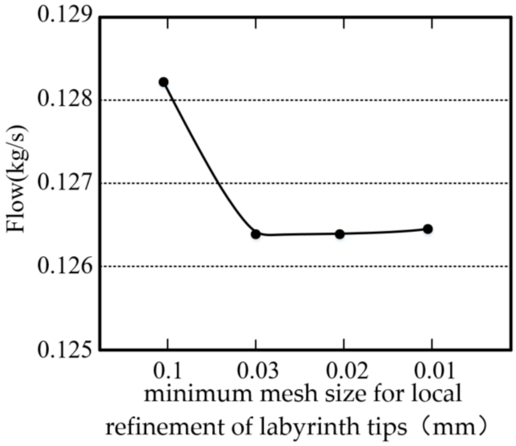

Figure 5. The minimum mesh size for local refinement independent computation.

3.3. Model Checking

In order to verify the accuracy of the parametric model, the calculation results of the simulation model in this paper were compared with the experimental data provided by known references [49]. The geometrical parameters of the labyrinth provided by the reference [50] are shown in Table 3. The data were input into the simulation model for calculating the leakage flow of the labyrinth under different inlet and outlet pressure ratios, and then we converted the leakage into the converted flow for comparison. The comparison results are shown in Table 4.

Table 3. Geometric parameters of the labyrinth.

Geometric Parameters	Symbol	Value	Unit
Seal clearance	c	0.36	mm
Tooth height	h	6	mm
Teeth pitch	L	6	mm
Tooth tip width	t	0.25	mm

Table 4. Comparison results.

SE. NU.	Pressure Ratio	Converted Flow $\varphi \times 10^2$						
		Test Results	Standard $k-\varepsilon$	Deviation	RNG $k-\varepsilon$	Deviation	SST $k-\omega$	Deviation
1	1.0357	0.7491	0.7813	4.29%	0.9567	27.71%	0.6659	−11.11%
2	1.0886	1.1621	1.2088	4.02%	1.4731	26.77%	1.0246	−11.83%
3	1.1598	1.5018	1.5467	2.99%	1.8720	24.65%	1.3265	−11.67%
4	1.2391	1.7480	1.7983	2.88%	2.1557	23.32%	1.5739	−9.96%
5	1.3878	2.0326	2.1025	3.44%	2.4773	21.88%	1.8981	−6.62%
6	1.4717	2.1616	2.2168	2.55%	2.5940	20.00%	2.0339	−5.91%
7	1.6290	2.3515	2.3816	1.28%	2.7448	16.72%	2.2314	−5.11%
8	1.7805	2.4116	2.4515	1.65%	2.8365	17.62%	2.3565	−2.28%
9	1.8974	2.4495	2.5106	2.50%	2.8872	17.87%	2.4371	−0.50%

In the present research, we briefly discussed the influence of various boundary conditions on the converted flow. It can be seen from Figure 6 that the converted flow was gradually increased with the increase of the pressure ratio. In addition, we can quantify that the conversion flow increased with the inlet temperature increase, and the conversion flow increased with the inlet pressure decrease from Equation (2).

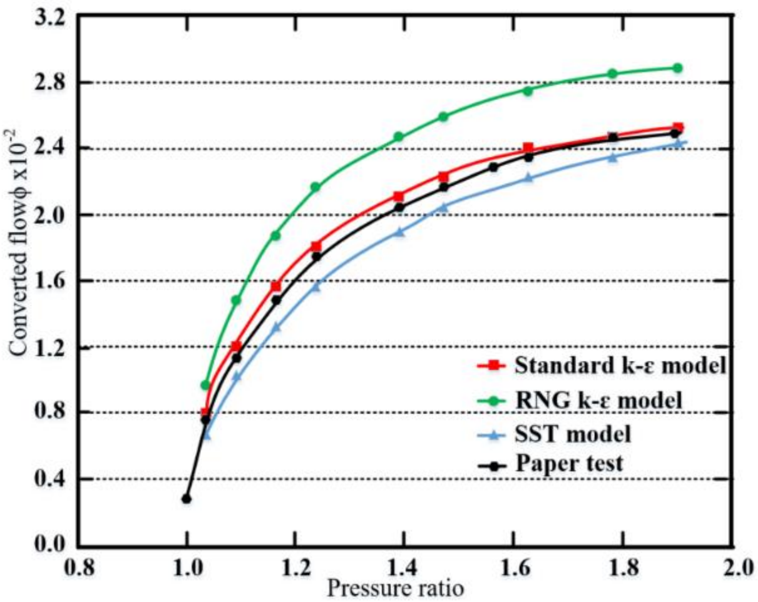

Figure 6. Comparison of turbulence models.

It can be seen from Table 4 that there were some differences in the calculation results obtained using the various turbulence models. In the calculated operating conditions, the maximum relative error of the converted flow was 4.29% which used the standard $k-\varepsilon$ turbulence model. Therefore, the standard $k-\varepsilon$ turbulence model was selected as the turbulence model for subsequent related calculations.

The results show that the calculation results of this paper are in fantastic agreement with the experimental results of the reference (Figure 7). In the working conditions, the maximum relative error of the converted flow rate was no more than 5%. The simulation model of the labyrinth established in this paper has high reliability.

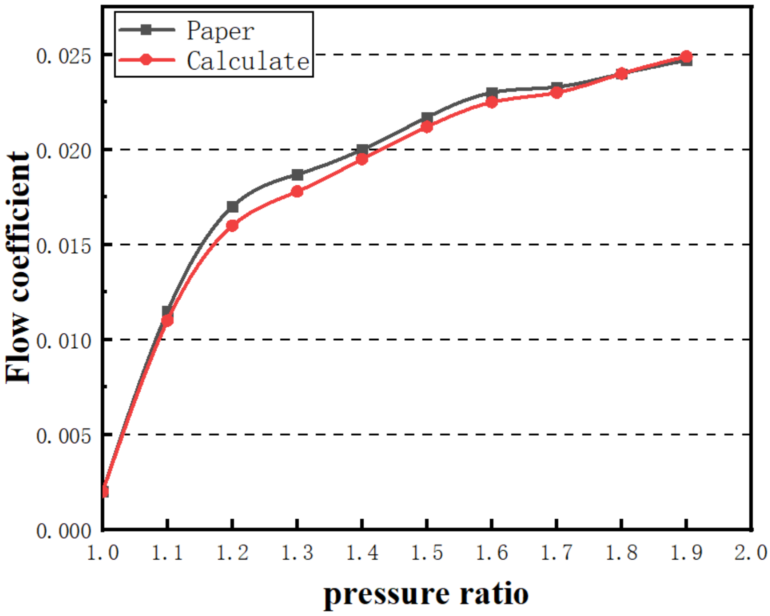

Figure 7. Comparison of calculation and reference test results.

4. Results and Discussion

In this section, the relationship between the FRIV and the relative dissipation intensity was first analyzed, being based on the theoretical research and simulation results. Then, the influence of the labyrinth tooth inclination angle, tooth tip width, step shape, and other parameters on the FRIV entropy generation were investigated. Finally, a more effective method to utilize the FRIV was proposed that is based on the research results.

4.1. The Formation Mechanism of FRIV

The flow field in the labyrinth region is shown in Figure 8. It can be seen that a high-speed airflow was formed in labyrinth region when the fluid flowed through the labyrinth teeth, which was mainly because of the strong throttling effect of the incoming flow at the tip. When the airflow passed through the labyrinth teeth, it suddenly expanded and was spread at a certain angle. Under the action of the flow resistance of the fluid in the labyrinth cavity and the frictional resistance of the wall surface, a vortex was formed in the labyrinth cavity.

Figure 9 shows the vorticity cloud map of the labyrinth, and Figure 10 shows the relative dissipation intensity distribution cloud map. Comparing and analyzing the two figures, we see that the distribution of the relative dissipative intensity was the same as the vorticity distribution, and it was mainly distributed on the wall and the tooth tip.

In order to express the correlation of the vorticity with the relative dissipative intensity distribution, we illustrated in Figure 11 the correlation coefficient cloud diagram, which was obtained by simulation. From the simulation results, it can be seen that there was a large correlation coefficient in the labyrinth tip. This result is consistent with the conclusion obtained from Equation (16), which indicates that there was a larger vortex. This vortex can be explained by the first term in Equation (17), which impeded the airflow at the tip and reduced leakage. When we input the vortex intensity ω obtained by simulation into Equation (18), it can be seen that the entropy generation increased exponentially.

4.2. Influence of Labyrinth Tip width Variation on Entropy Generation

The labyrinth teeth with the labyrinth tip widths of 0.2, 0.4, 0.6, and 0.8 mm were selected for comparative research. Figure 12 shows the flow field for different labyrinth tip widths. Figure 13 shows the distribution of entropy generation for different labyrinth tip widths.

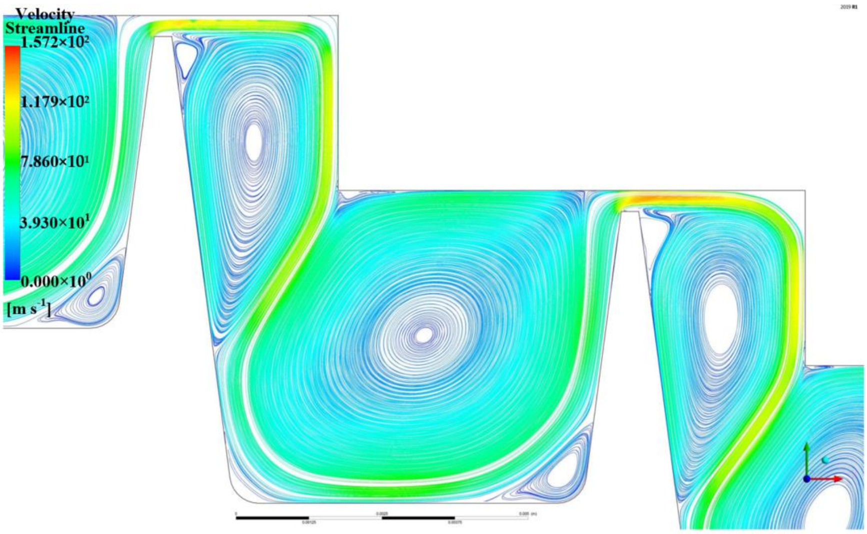

Figure 8. Formation diagram of the FRIV.

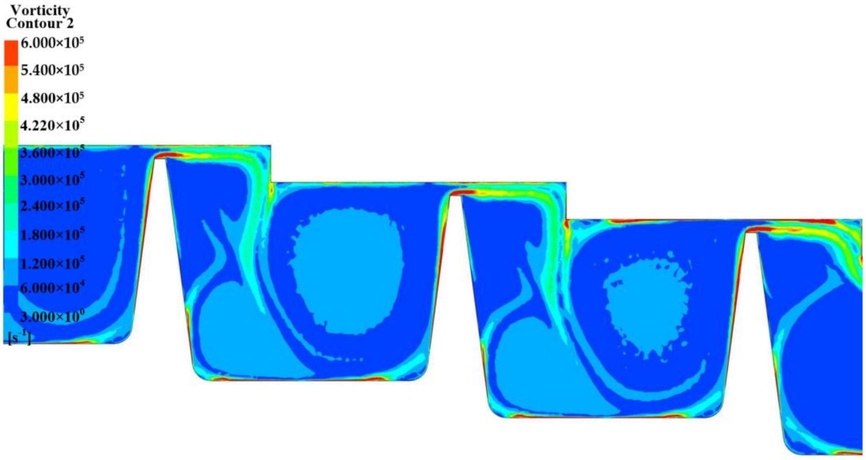

Figure 9. Cloud map of vorticity distribution.

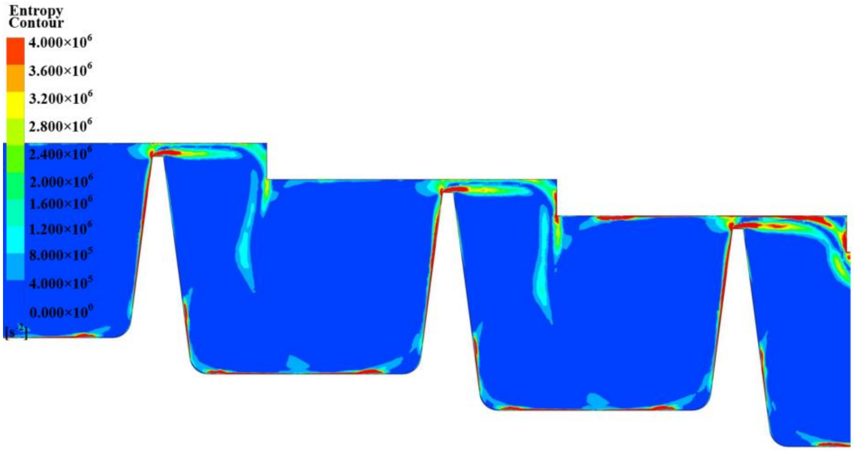

Figure 10. Cloud map of relative dissipative intensity distribution.

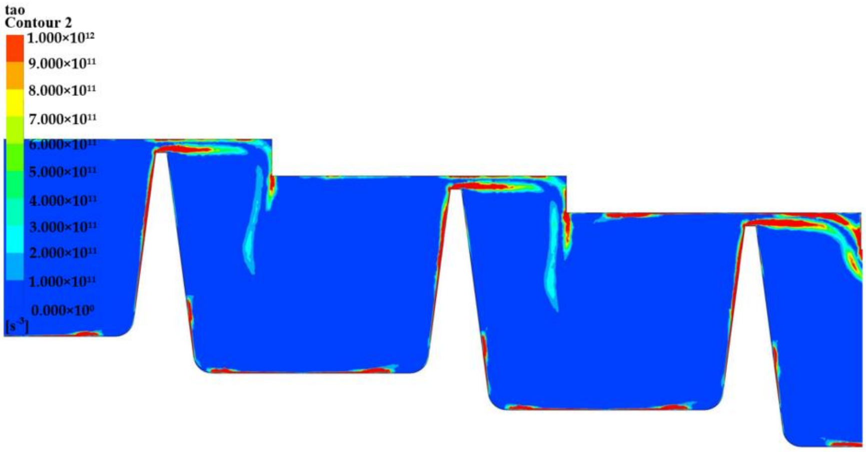

Figure 11. Correlation coefficient distribution.

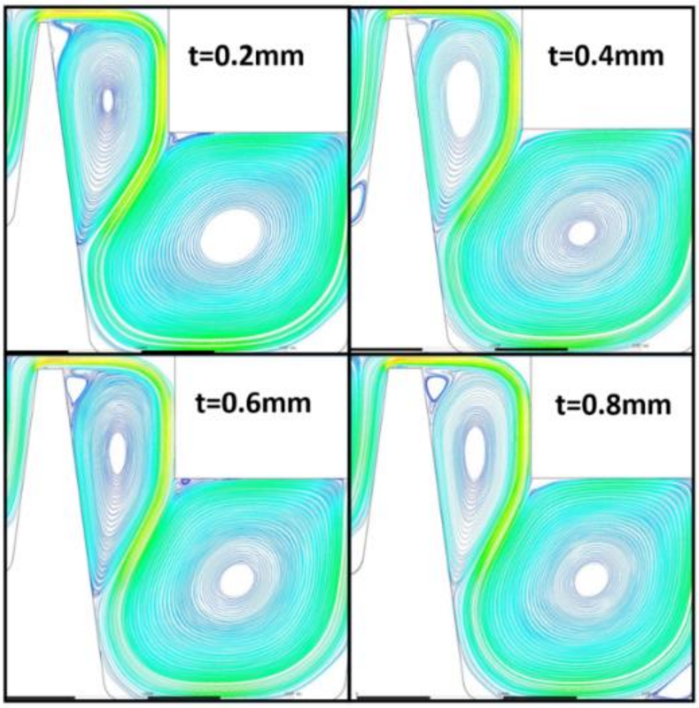

Figure 12. Flow field for different tip widths.

It can be seen from Figure 12 that with the increase of labyrinth width, the direction of airflow velocity was gradually reversed, and the strength of the FRIV was weakened. It can be seen from Equation (14) that ϕ may be decreased with the increase of the labyrinth tip width, and the relative dissipative strength decreased with the increase of the tip width. It can be seen from Equation (15) that the vortex strength decreased with the increase of the tip width and the influence of the vortex became weaker when the tip width was larger. When the tip width was small, the gas flow direction changed rapidly after the gas in the upper labyrinth cavity flowed through the tip, where the velocity gradient was large. This result was consistent with the conclusion in Equation (17) that the vortex was stretched and bent due to the velocity gradient of the flow field, which led to changes in the magnitude and direction of the vorticity. In addition, the major flow in the tip area may be affected by the extrusion of the vortex on the rear side of the labyrinth tooth tip. When the tooth tip width of the labyrinth was smaller, the vortex on the rear side of the tooth tip was stronger, which strengthened the influence on the flow in the tooth tip area and strengthened the compression effect of the tooth tip gap. Further, the flow field data (as shown in Figure 12) obtained by the simulation was output and substituted into the entropy generation of Equations (15) and (18). The relationship between the entropy generation and the airflow position can be obtained. It can be seen from Figure 14 that the results are consistent with the variation of entropy generation with tooth tip width (as shown in Figure 13).

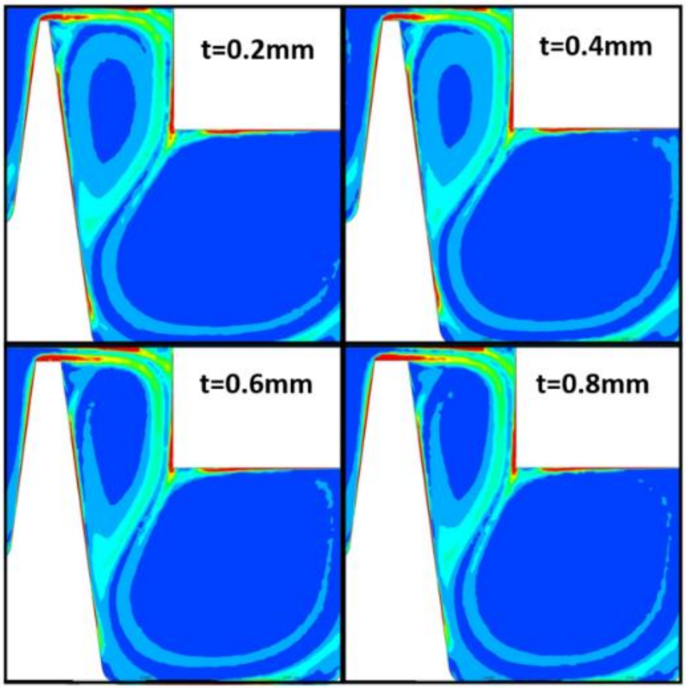

Figure 13. The distribution of entropy generation with different tip widths.

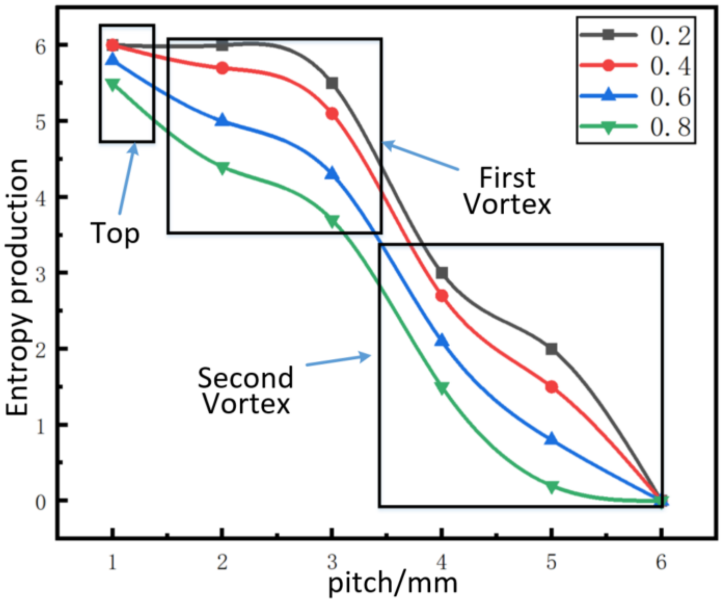

Figure 14. Variation of entropy generation with airflow position.

In conclusion, in the labyrinth tip, the entropy generation was the largest; with the increase of tooth tip width, the entropy generation of the FRIV gradually decreased.

4.3. Influence of Labyrinth Inclination on Entropy Generation

The labyrinth inclination angle α from 50° to 120° is divided into 8 groups for comparative research. Figure 15 shows the effect of different Labyrinth inclination angles on the vortex strength, Figure 16 shows the effect of different labyrinth inclination angles on the flow field.

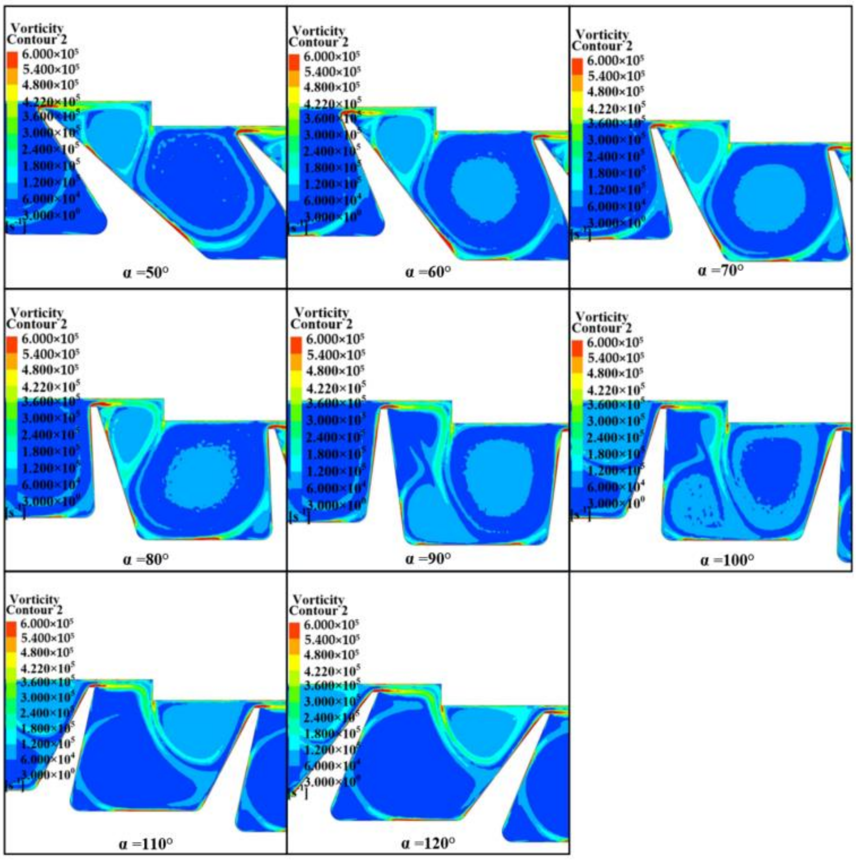

Figure 15. Distribution of the vortex with the change of the labyrinth inclination angle.

It can be seen from Figure 16 that when the labyrinth teeth were inclined forward, the FRIV on the top of the teeth increased significantly compared to the vertical position of the labyrinth teeth. The flow-resistance-increasing vortices almost occupied the clearance, which is beneficial to the sealing of the labyrinth. When the labyrinth teeth were inclined backward, the FRIV on the top of the labyrinth gradually weakened, being transferred to the low radius of the labyrinth back, forming two vortexes in the labyrinth cavity. In terms of the cloud image data shown in Figures 15 and 16, the trend diagram of the vortex intensity with the labyrinth inclination angle was obtained, as shown in Figure 17.

Figure 17 illustrates the labyrinth vortex and the thickness of vortex as a function of labyrinth inclination. It can be seen from Figure 17 that with the labyrinth inclination decreasing, the vortex increased, and the thickness of the vortex increased, indicating that the FRIV of the labyrinth was gradually strengthened. The FRIV occupied the radial clearance of the labyrinth and hindered the flow. When the labyrinth inclination angle was less than 60°, the growth trend of the vortex slowed down, and the thickness of the vortex remained stable. This result is consistent with the conclusion from the qualitative analysis of Equation (17). When the inclination angle became smaller, the velocity and direction of the flow field changed more greatly, which caused the velocity gradient in the flow field to change significantly and led to the change of the absolute value of the vorticity. As a result, the FRIV effect was enhanced accordingly.

4.4. Influence of Step Inclination Angle Change on Entropy Generation

Taking the labyrinth inclination angle of 60 degrees, the labyrinth teeth with step inclination angles of 60°, 70°, 80°, and 90° were selected for comparative research. Figures 18 and 19 show the flow field diagram and the entropy generation diagram in the labyrinth with different step inclination angles, respectively.

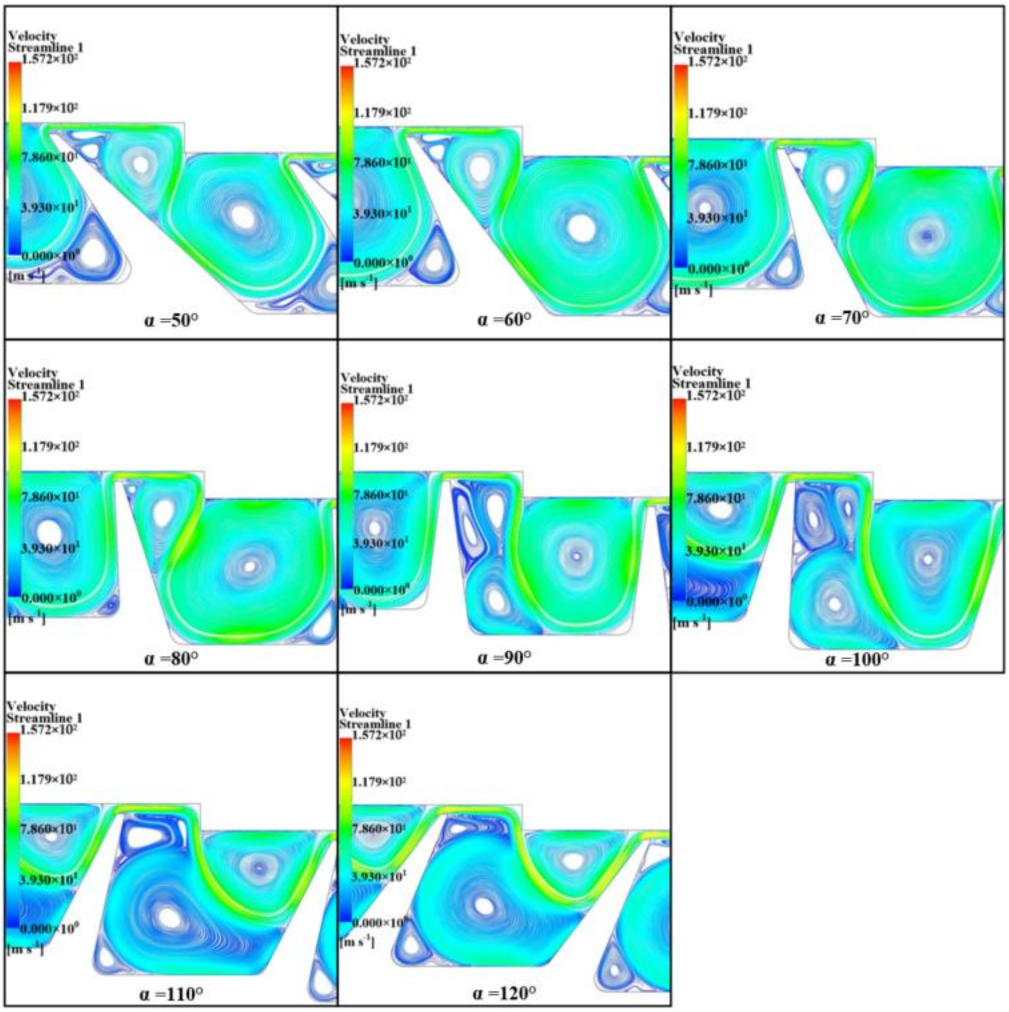

Figure 16. Flow field with the change of labyrinth inclination angle.

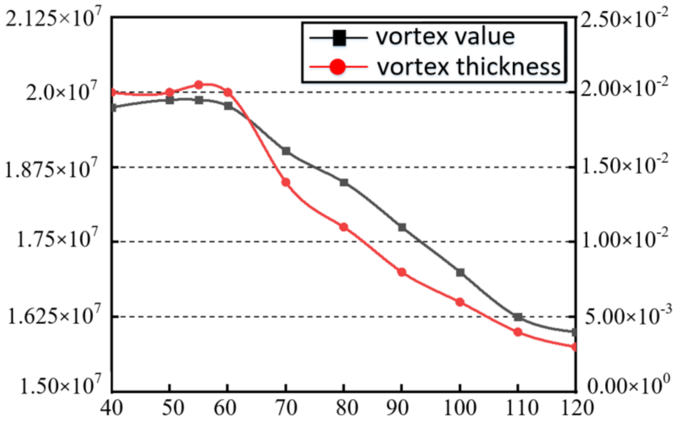

Figure 17. The trend of vortex with labyrinth inclination change.

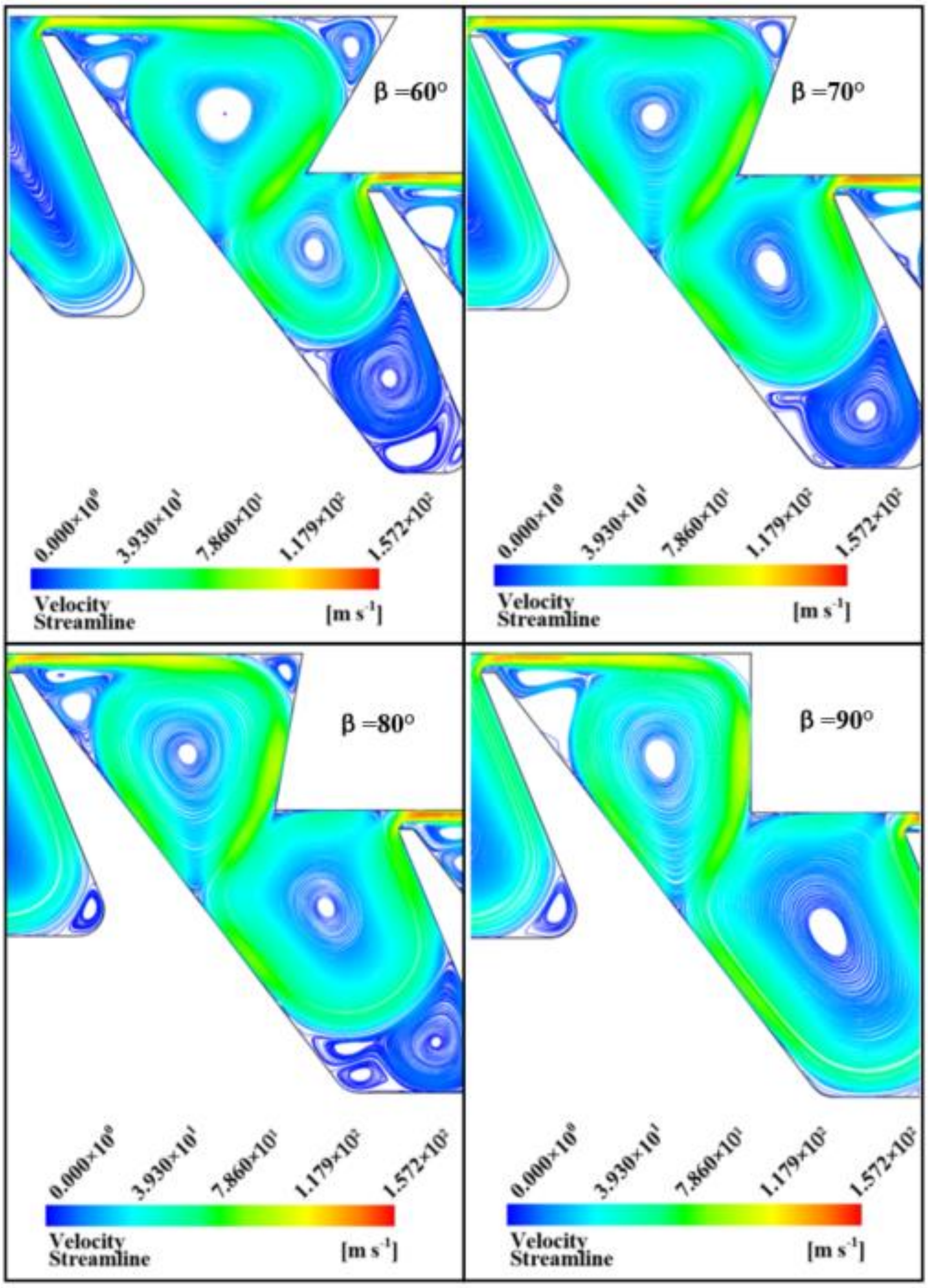

Figure 18. Flow field diagram with different step inclinations.

It can be seen from Figure 18 that the incoming flow through the labyrinth tip directly hit the step wall and then changed the flow direction, which flowed to the labyrinth cavity along the inclined angle of the step. Then, the air flow was divided into two parts, and two opposite vortices were formed at the inner step of the labyrinth and in the tooth cavity. As the inclination angle of the step decreased, the vortex at the inner step of the labyrinth was squeezed toward the labyrinth tip and increased. This result is consistent with the conclusion drawn from the second item in Equation (17). Due to the decrease of the inclination angle, the volume change rate of the airflow in the tooth tip became larger, which caused the absolute value of the vorticity to increase. Further, the flow field data in Figure 18 were substituted into the entropy generation Equations (15) and (18), wherein the relationship between the entropy generation and the airflow position as shown in Figure 20 can be obtained. It can be seen from Figure 20 that this result was consistent with the result

(Figure 19) of the simulation. In other words, with the increase of the inclination angle of the step, the entropy generation of the FRIV gradually decreased.

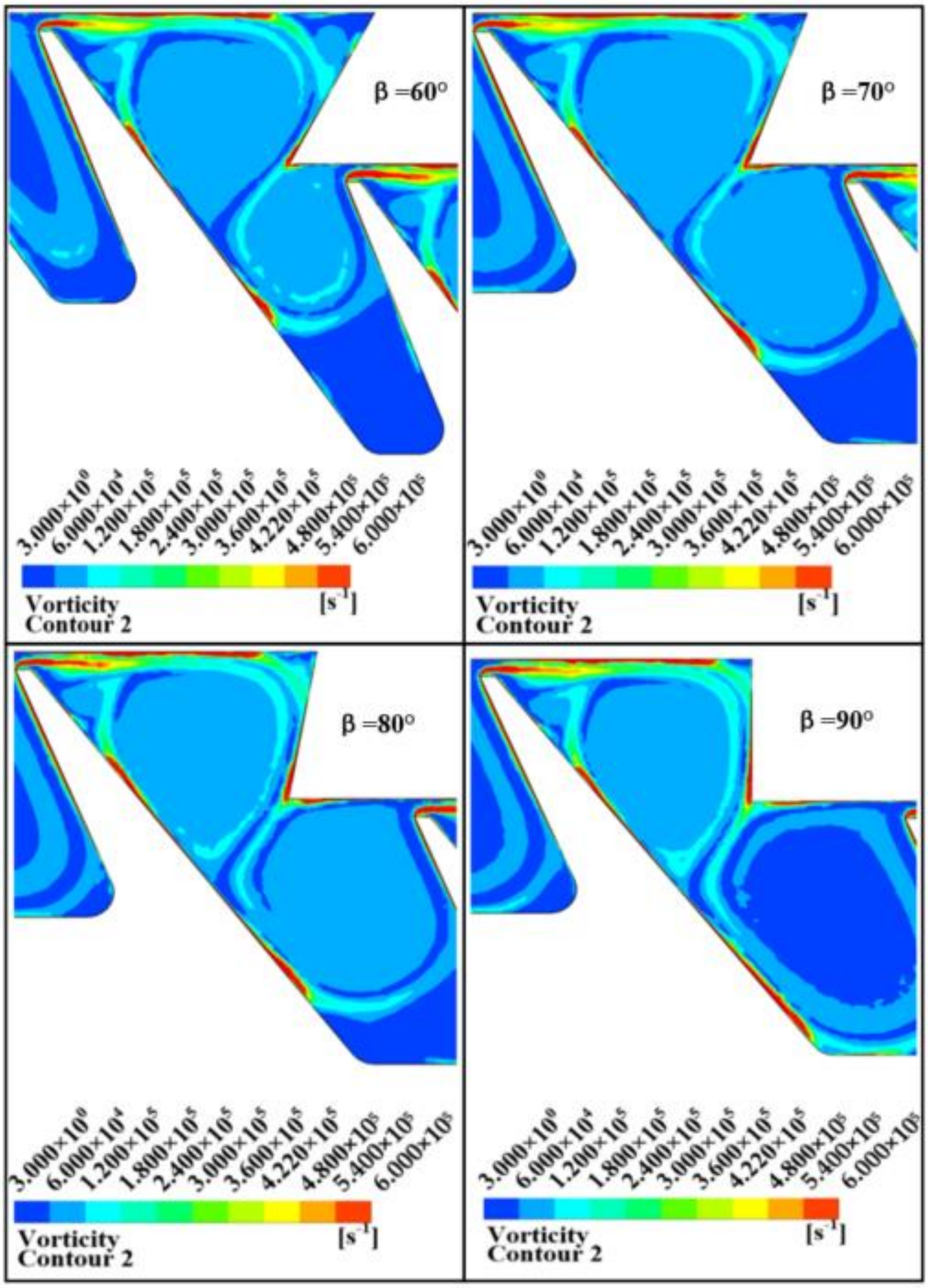

Figure 19. Distribution of the entropy generation with different step inclinations.

4.5. Influence of FRIV Strength on Leakage

In this paper, a stronger FRIV was constructed on the basis of the influence of geometric parameter changes on entropy production [51,52], which is defined as the best; the geometric parameters are shown in Table 5. The best entropy generation was studied and compared with the initial FRIV. Figure 21 shows the comparison flow field between the best and the initial. Figure 22 shows the comparison distribution of FRIV entropy generation between the best and the initial.

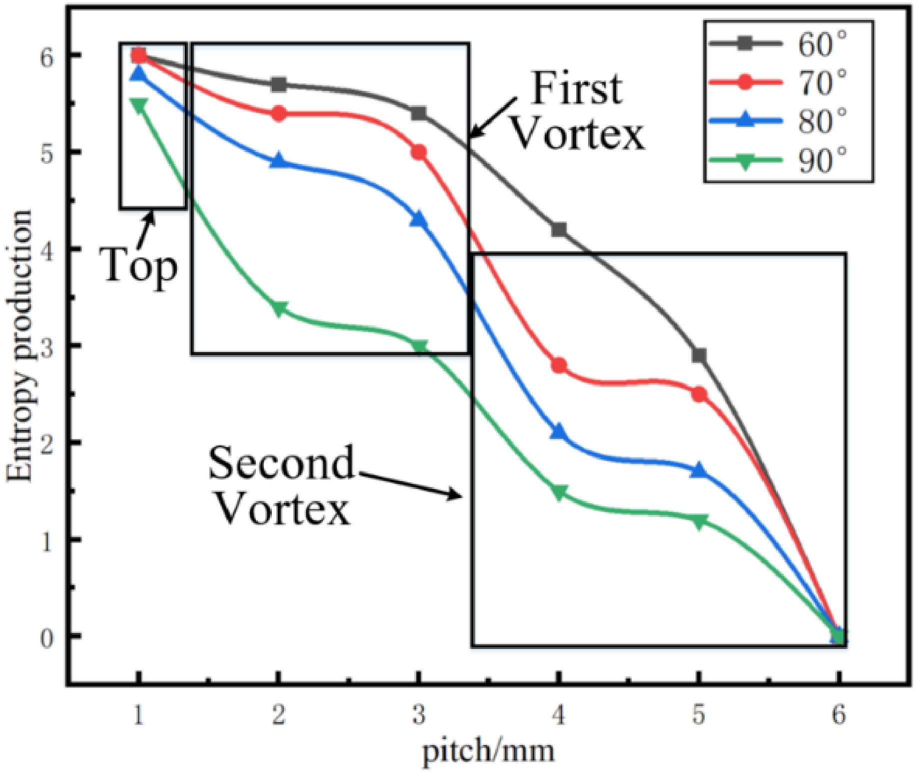

Figure 20. Entropy generation with step inclination change.

Table 5. The best labyrinth geometry parameters.

Geometrical Parameters	Symbol	Initial Value	Unit
Step height	H	2	mm
Tooth spacing	L	7	mm
Tooth height	h	5	mm
Tooth tip width	t	0.2	mm
Labyrinth inclination angle	α	60	degrees
Angle between face teeth	θ	15	degrees
Seal clearance	c	0.36	mm
Tooth to step distance	b	2	mm
Step inclined angle	β	60	degrees
Root rounding of steps	R1	0	mm
Root rounding on pressure side	RL	0.5	mm
Fin tip fillet	RR	0.5	mm

It can be seen from Figure 22 that the best entropy production was larger. From the calculation results in Table 6, the best flow rate through the top of the labyrinth teeth was reduced by 22%, which verifies the fact that the sealing effect of the labyrinth structure became stronger. The calculation results of entropy generation and leakage flow rate illustrate the fact that the method proposed in this study is effective in reducing the leakage of labyrinth teeth.

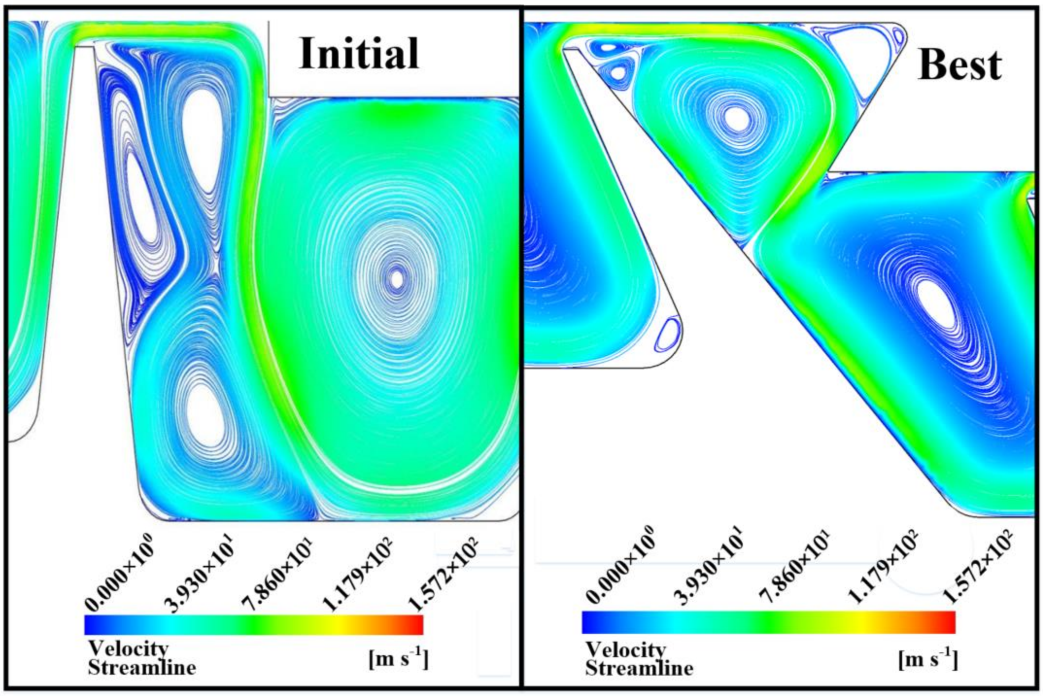

Figure 21. Flow field comparison diagram.

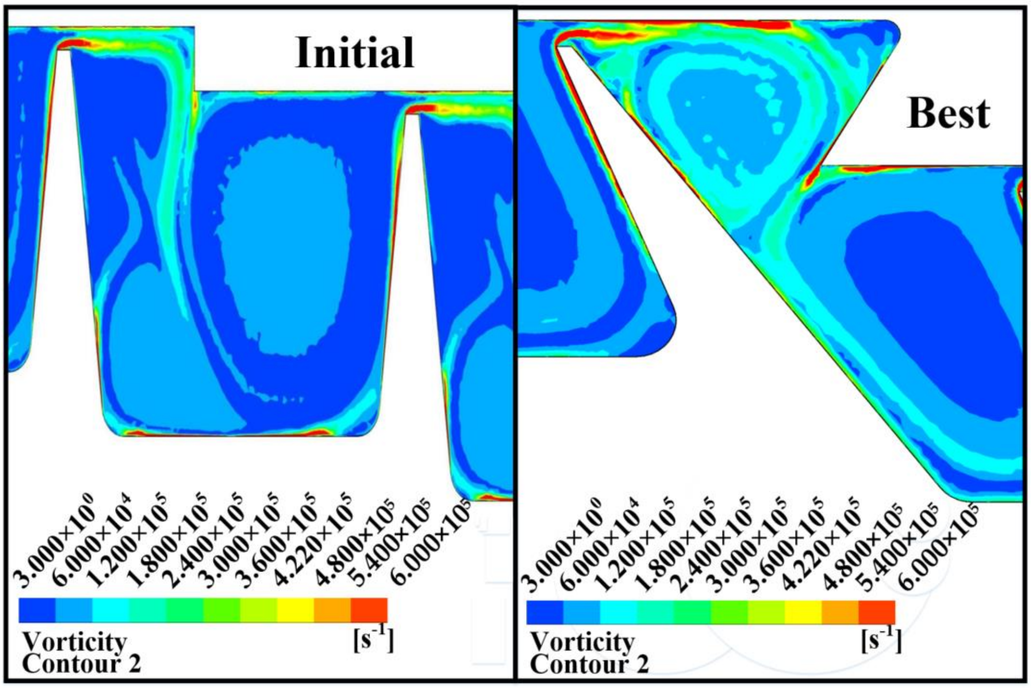

Figure 22. Comparison of entropy generation distribution.

Table 6. Calculation results.

Serial Number	Pressure Ratio	Standard $k-\varepsilon$	Best	Degree of Reduction
1	1.0357	0.7813	0.6124	21.6%
2	1.0886	1.2088	0.9546	21.02%
3	1.1598	1.5467	1.2565	18.76%
4	1.2391	1.7983	1.5239	15.25%
5	1.3878	2.1025	1.8981	12.09%
6	1.4717	2.2168	2.0339	10.50%
7	1.6290	2.3816	2.2314	8.4%
8	1.7805	2.4515	2.3565	5.91%
9	1.8974	2.5106	2.4371	4.91%

5. Conclusions

In this paper, the modeling and simulation of the aero-engine labyrinth structure was carried out, and the model was checked according to the known experimental data. The concept of FRIV was proposed, and the influence of related geometric parameters on the entropy generation of FRIV was studied.

(1) The relative dissipative intensity distribution was the same as the vorticity distribution, and there was a region with a large correlation coefficient at the top of the tooth, where the vortex was stronger and the dissipation effect was stronger.

(2) When the labyrinth width was small, the flow direction changed rapidly after the gas in the upper labyrinth cavity flowed into the labyrinth tip, which formed a FRIV at the labyrinth tip. With the increase of tooth width, the direction of fluid velocity was gradually reversed. In addition, the entropy generation and the resistance increase effect were weakened. When the labyrinth teeth were inclined forward, the FRIV on the top of the tooth increased significantly, and the entropy generation increased, almost occupying the entire labyrinth clearance. When the labyrinth teeth were inclined backward, the FRIV on the top of the tooth gradually weakened. As the inclination angle of the step decreased, the vortex at the inner step of the labyrinth squeezed toward the tooth tip and increased. In addition, the FRIV was enhanced, the entropy generation increased, and the sealing effect was strengthened.

(3) By selecting reasonable labyrinth geometric parameters, the labyrinth tip velocity gradient and throttling effect can be enhanced, and the $(\omega\cdot\nabla)V$ and $\omega(\nabla\cdot V)$ terms in the vorticity transport equation can be increased, which can strengthen FRIV and reduce leakage. The results of this research show that the reasonable labyrinth parameters can reduce leakage by 22%. Therefore, the method of reducing leakage proposed in this paper is effective.

Author Contributions: Methodology, X.L.; validation, S.D. and L.S.; formal analysis, X.Z.; investigation, S.Z. and G.L.; resources, T.Q.; writing—original draft preparation, Y.Z. All authors have read and agreed to the published version of the manuscript.

Funding: This work was funded by the Basic Research Program of the National Nature Science Foundation of China, grant number 51775025 and 51775013, China Key Research and Development Plan (No.2017YFB0102102, 2018YFB0104100).

Institutional Review Board Statement: Not applicable.

Informed Consent Statement: Not applicable.

Data Availability Statement: The data used to support the findings of this study are included within the article.

Acknowledgments: The Basic Research Program of the National Nature Science Foundation of China, grant number 51775025 and 51775013, China Key Research and Development Plan (No.2017YFB0102102, 2018YFB0104100).

Conflicts of Interest: The authors declare no conflict of interest.

References

1. Ludwig, L.P.; Johnson, R.L. *Sealing Technology for Aircraft Gas Turbine Engines*; AIAA: Reston, VA, USA, 2000.
2. Guo, H.; Feng, Q. Experiment on flow characteristic in rotating labyrinth with consideration of clearance change. *J. Aerosp. Power* **2018**, *33*, 1779–1786.
3. Hanzlik, H.J. Labyrinth Packing. US1831242A, 10 November 1931.
4. Vermes, G.Z. A Fluid Mechanics Approach to the Labyrinth Seal Leakage Problem. *J. Eng. Gas Turbines Power* **1960**, *83*, 161. [CrossRef]
5. Zimmermann, H.; Wolff, K.H. Air System Correlations: Part 1—Labyrinth Seals. In Proceedings of the Asme International Gas Turbine & Aeroengine Congress & Exhibition, Stockholm, Sweden, 2 June 1998.
6. Nayak, K.C. Effect of Rotation on Leakage and Windage Heating in Labyrinth Seals With Honeycomb Lands. *J. Eng. Gas Turbines Power* **2020**, *142*, 081001. [CrossRef]
7. Lee, S.I.; Kang, Y.J. Basic Research Trends on Labyrinth Seal of Gas Turbine. *KSFM J. Fluid Mach.* **2020**, *23*, 32–39. [CrossRef]
8. Soemarwoto, B.I.; Kok, J.C. Performance Evaluation of Gas Turbine Labyrinth Seals Using Computational Fluid Dynamics. In Proceedings of the ASME Turbo Expo 2007: Power for Land, Sea, and Air, Montreal, QC, Canada, 14–17 May 2007; Volume 4.
9. Rhode, D.L.; Demko, J.A. Prediction of Incompressible Flow in Labyrinth Seals. *J. Fluids Eng.* **1986**, *108*, 19–25. [CrossRef]
10. Demko, J.A.; Morrison, G.L.; Rhode, D.L. The Prediction and Measurement of Incompressible Flow in a Labyrinth Seal. *J. Eng. Gas Turbines Power* **1989**, *111*, 189–195. [CrossRef]
11. Stoff, H. Incompressible flow in a labyrinth seal. *J. Fluid Mech.* **2006**, *100*, 817–829. [CrossRef]
12. Rhode, D.L.; Sobolik, S.R. Simulation of Subsonic Flow Through a Generic Labyrinth Seal. *J. Eng. Gas Turbines Power* **1985**, *108*, 429–437. [CrossRef]
13. Rhode, D.L.; Hibbs, R.I. New model for flow over open cavities. I-Model development. *J. Propuls. Power* **1992**, *8*, 392–397. [CrossRef]
14. Rhode, D.L.; Hibbs, R.I. New model for flow over open cavities. II-Assessment for seal leakage. *J. Propuls. Power* **1971**, *8*, 398–402. [CrossRef]
15. Demko, J.A.; Morrison, G.L. Effect of shaft rotation on the incompressible flow in a labyrinth seal. *J. Propuls. Power* **1990**, *6*, 171–176. [CrossRef]
16. Rapisarda, A.; Desando, A. Rounded Fin Edge and Step Position Effects on Discharge Coefficient in Rotating Labyrinth Seals. *J. Turbomach.* **2016**, *138*, 011005. [CrossRef]
17. Scherer, T.; Waschka, W. Numerical Predictions of High-Speed Rotating Labyrinth Seal Performance: Influence of Rotation on Power Dissipation and Temperature Rise. In *International Symposium on Heat Transfer in Turbomachinery*; Begell House Inc.: Danbury, CT, USA, 1994.
18. Nayak, K.; Ansari, A. The Effect of Rub-Grooves on Leakage and Windage Heating in Labyrinth Seals with Honeycomb Lands. In Proceedings of the Aiaa/Asme/Sae/Asee Joint Propulsion Conference & Exhibit, San Jose, CA, USA, 14–17 July 2013.
19. Musthafa, K.C. The Effects of Tooth Tip Wear and its Axial Displacement in Rub-Grooves on Leakage and Windage Heating of Labyrinth Seals with Honeycomb Lands. In Proceedings of the 43rd AIAA/ASME/SAE/ASEE Joint Propulsion Conference & Exhibit (AIAA), Nashville, TN, USA, 8–11 July 2007.
20. Kaliraj, K.R.; Yepuri, G.B. Parametric Studies on Gas Turbine Labyrinth Seal for the Secondary Air Flow Optimization at Static and Rotating Conditions. In Proceedings of the ASME 2019 Gas Turbine India Conference, Chennai, India, 5–6 December 2019.
21. Desando, A.; Rapisarda, A. Numerical Analysis of Honeycomb Labyrinth Seals:Cell Geometry and Fin Tip Thickness Impact on the Discharge Coefficient. In Proceedings of the ASME Turbo Expo 2015, Montreal, QC, Canada, 15–19 June 2015.
22. Ganine, V.; Chew, J.W. Transient Aero-Thermo-Mechanical Multidimensional Analysis of a High Pressure Turbine Assembly Through a Square Cycle. *J. Eng. Gas Turbines Power* **2021**, *143*, 081008. [CrossRef]
23. Childs, D.W. Turbomachinery Rotordynamics: Phenomena, Modeling, and Analysis. In *Turbomachinery Rotordynamics Phenomena Modeling and Analysis*; John Wiley and Sons: Hoboken, NJ, USA, 1993.
24. Wittig, S.L.; Dörr, K.L. Scaling Effects on Leakage Losses in Labyrinth Seals. *J. Eng. Gas Turbines Power* **1983**, *105*, 305–309. [CrossRef]
25. Denecke, J.; Dullenkopf, K. Experimental Investigation of the Total Temperature Increase and Swirl Development in Rotating Labyrinth Seals. In Proceedings of the Asme Turbo Expo: Power for Land, Sea, & Air, Reno, NV, USA, 6–9 June 2005.
26. Mcgreehan, W.F.; Ko, S.H. Power Dissipation in Smooth and Honeycomb Labyrinth Seals. In Proceedings of the ASME 1989 International Gas Turbine and Aeroengine Congress and Exposition, Toronto, ON, Canada, 4–8 June 1989.
27. Willenborg, K.; Kim, S. Effects of Reynolds Number and Pressure Ratio on Leakage Loss and Heat Transfer in a Stepped Labyrinth Seal. *J. Turbomach.* **2001**, *123*, 815. [CrossRef]
28. Stocker, H.L.; Cox, D.M. *Aerodynamic Performance of Conventional and Advanced Design Labyrinth Seals with Solid-Smooth Abradable, and Honeycomb Lands*; NASA: Washington, DC, USA, 1977; pp. 1–272.
29. Rhode, D.L.; Adams, R.G. Rub-Groove Width and Depth Effects on Flow Predictions for StraightThrough Labyrinth Seals. *J. Tribol.* **2004**, *126*, 781–787. [CrossRef]

30. Millward, J.A.; Edwards, M.F. Windage Heating of Air Passing Through Labyrinth Seals. *J. Turbomach.* **1996**, *118*, 414–419. [CrossRef]
31. Waschka, W.; Wittig, S. Influence of High Rotational Speeds on the Heat Transfer and Discharge Coefficients in Labyrinth Seals. *J. Turbomach.* **1990**, *114*, 462–468. [CrossRef]
32. Braun, E.; Dullenkopf, K. Optimization of Labyrinth Seal Performance Combining Experimental, Numerical and Data Mining Methods. In Proceedings of the Asme Turbo Expo: Turbine Technical Conference & Exposition, Copenhagen, Denmark, 11–15 June 2012.
33. Min, S.H.; Soo, I.L. Effect of clearance and Cavity Geometries on Leakage Performance of a Stepped Labyrinth Seal. *Processes* **2020**, *8*, 1496.
34. Khan, N.S.; Shah, Q. Mechanical aspects of Maxwell nanofluid in dynamic system with irreversible analysis. *ZAMM J. Appl. Math. Mech.* **2021**, *101*, e202000212. [CrossRef]
35. Ramzan, M.; Khan, N.S. Mechanical analysis of non-Newtonian nanofluid past a thin needle with dipole effect and entropic characteristics. *Sci. Rep.* **2021**, *11*, 19378. [CrossRef] [PubMed]
36. Yu, Z.; Lifeng, H. Investigation on transient dynamics of rotor system in air turbine starterbased on magnetic reduction gear. *J. Adv. Manuf. Sci. Technol.* **2021**, *1*, 2021009. [CrossRef]
37. Jiang, W.; Bin, W. A Novel Blade Tip Clearance Measurement Method Based on Event Capture Technique. *Mech. Syst. Signal Process.* **2020**, *139*, 106626.
38. Weinberger, T.; Dullenkopf, K. Influence of Honeycomb Facings on the Temperature Distribution of Labyrinth Seals. In Proceedings of the ASME Turbo Expo 2010: Power for Land, Sea, and Air, Glasgow, UK, 14–18 June 2010.
39. Shuiting, D.; Ziyao, W. Probabilistic failure risk assessment for aeroengine disks considering a transient process. *Aerosp. Sci. Technol.* **2018**, *78*, 696–707.
40. Ding, S.; Che, W. Application of entropy equation in the judgement of flow direction in transient air system. *J. Aerosp. Power* **2017**, *32*, 2305–2313.
41. Bertin, J.; Cummings, R. *eBook Instant Access—for Aerodynamics for Engineers, International Edition*; Pearson: London, UK, 2013.
42. Allahverdyan, A.; Nieuwenhuizen, T. Steady adiabatic state: Its thermodynamics, entropy production, energy dissipation, and violation of Onsager relations. *Phys. Rev. E* **2000**, *62*, 845. [CrossRef]
43. Denecke, J.; Frber, J. Dimensional Analysis and Scaling of Rotating Seals. In Proceedings of the ASME Turbo Expo 2005: Power for Land, Sea, and Air. 2005, Reno, NV, USA, 6–9 June 2005.
44. Dagan, A.; Arieli, R. Solutions of the vorticity transport equation at high Reynolds numbers. In Proceedings of the Thirteenth International Conference on Numerical Methods in Fluid Dynamics, Rome, Italy, 6–10 July 1992.
45. Koh, Y.M. Vorticity and viscous dissipation in an incompressible flow. *KSME J.* **1994**, *8*, 35–42. [CrossRef]
46. Barati, R. The numerical solution of the vorticity transport equation. In Proceedings of the Third International Conference on Numerical Methods in Fluid Mechanics, Paris, France, 7 July 1972.
47. ANSYS Inc. *ANSYS CFX 19.0*; ANSYS Inc.: Canonsburg, PA, USA, 2018.
48. Yu, Z.; Longtao, S. Numerical and Experimental Investigation on Dynamic performance of Bump Foil Journal Bearing Based on Journal Orbit. *Chin. J. Aeronaut.* **2021**, *34*, 586–600.
49. ANSYS Inc. *ANSYS CFX-Solver Modeling Guide*; ANSYS Inc.: Canonsburg, PA, USA, 2011.
50. Prasad, B.V.S.S.; Manavalan, V.S. Computational and Experimental Investigations of Straight-Through Labyrinth Seals. In Proceedings of the Asme International Gas Turbine & Aeroengine Congress & Exhibition, Orlando, FL, USA, 2 June 1997.
51. Yu, Z.; Tong, X. Digital-twin-driven geometric optimization of centrifugal impeller with free-form blades for five-axis flank milling. *J. Manuf. Syst.* **2021**, *58*, 22–35.
52. Yu, Z.; Yue, S. Parametric Modeling Method for Integrated Design and Manufacturing of Radial Compressor Impeller. *Int. J. Adv. Manuf. Technol.* **2020**, *10*, 1178.